npj | 2D materials and applications

www.nature.com/npj2dmaterials

ARTICLE OPEN

# Van der Waals interfaces in multilayer junctions for ultraviolet photodetection

Shihong Xie[1,2]✉, Mustaqeem Shiffa[1], Mujahid Shiffa[1], Zakhar R. Kudrynskyi[1], Oleg Makarovskiy[1], Zakhar D. Kovalyuk[3], Wenkai Zhu[2], Kaiyou Wang[2] and Amalia Patanè[1]✉

Developments in semiconductor science have led to the miniaturization and improvement of light detection technologies for many applications. However, traditional *pn*-junctions or three-dimensional device geometries for detection of ultraviolet (UV) light are still limited by the physical properties of the semiconductors used, such as the small penetration depth of UV light in silicon. Van der Waals (vdW) semiconductors and their *pn*-junctions can offer an alternative solution due to their optical properties and thin *pn*-junction region. Here, we report on a multi-layer junction that combines single layer graphene and vdW semiconductors (*p*-GaSe and *n*-$In_2Se_3$) with strong optical absorption in the UV range. The junctions have broadband spectral response (0.3-1.0 μm) and high photoresponsivity under forward and reverse bias, or without any externally applied voltage. The photoresponse differs from that of a traditional *pn*-junction diode as it is governed by charge transport across thin layers and light-current conversion at three vdW interfaces (e.g. the graphene/GaSe, GaSe/$In_2Se_3$ and $In_2Se_3$/graphene interfaces). The type-II band alignment at the GaSe/$In_2Se_3$ interface and electric field at the three vdW interfaces are beneficial to suppress carrier recombination for enhanced photoresponsivity (up to ~$10^2$ A/W) and detectivity (up to ~$10^{13}$ Jones), beyond conventional UV-enhanced silicon detection technology.

*npj 2D Materials and Applications* (2022)6:61 ; https://doi.org/10.1038/s41699-022-00338-0

## INTRODUCTION

Photodetectors have potential for several applications, ranging from communication, aerospace and military technologies to pharmaceutical research[1]. However, high-performance photodetection over a range that extends into the ultraviolet (UV) range has proven to be challenging. Traditional Si-based thin-film technologies tend to underperform at short wavelengths due to a low optical absorption[2–4]. Alternative devices, such as photomultiplier tubes (PMTs), charged-coupled devices (CCDs) and semiconductor photodiodes[1,5,6], can achieve higher absorption in the UV range but at the cost of a slow photoresponse, high power consumption and/or low efficiency[6–8]. Two-dimensional (2D) van der Waals (vdW) semiconductors offer an alternative solution. They have tuneable absorption and fast temporal responses at room temperature while remaining flexible and power efficient[9–15]. They also possess surfaces that are free of dangling bonds leading to a low density of interface traps and the formation of high-quality heterostructure devices without the need for lattice matching[16]. Thus, multi-layer vdW heterostructures could be used to enhance the performance of a photodetector by exploiting the optical properties of different materials and the unique effects that arise from their interactions, such as charge transfer, built-in electric fields, and moiré superlattices[17–20].

Among the wide catalogue of 2D materials, the III–VI metal chalcogenide (MC) compounds have emerged as an ideal class of semiconductors for optoelectronics[9,21–23]. High-performance photodetectors based on individual flakes of either GaSe or $In_2Se_3$ have been reported before[21,23–25]. These two 2D MC layers have optical band gaps in the visible (GaSe)[8] and in the near-infrared ($In_2Se_3$) spectral range[26], and strong absorption in the UV region[21,27–29]. Thus, photodiodes based on multiple photon absorbing layers, such as GaSe and $In_2Se_3$, and/or their *pn*-junctions are well suited for broadband detection that extends into the UV range. However, the operation of a *pn*-junction based on 2D materials can differ qualitatively from that of a traditional semiconductor diode and may not be suitable for high-sensitivity photodetection due to large dark currents and interlayer carrier recombination[30–32].

In this work, we report on graphene/*p*-GaSe/*n*-$In_2Se_3$/graphene heterostructures where a *p*-GaSe/*n*-$In_2Se_3$ junction and two graphene electrodes are vertically stacked. These devices have photoresponsivity that extends into the UV range under both forward and reverse bias, or without any externally applied voltage. The bias-dependent photoresponsivity differs from that of a conventional *pn*-junction and arises from photon-current conversion at the three interfaces of the heterostructure (i.e. graphene/GaSe, GaSe/$In_2Se_3$ and graphene/$In_2Se_3$ interfaces) with graphene acting as an optically transparent electrode and efficient carrier collector, and the GaSe and $In_2Se_3$ layers providing the photon absorbers. Furthermore, the type-II band alignment of the GaSe/$In_2Se_3$ heterostructure and the electric field at the three vdW interfaces are beneficial to suppress carrier recombination in the junction for enhanced photoresponsivity and detectivity, comparable to that of state-of-the-art photodetectors.

## RESULTS AND DISCUSSION

### Photodetectors based on graphene-contacted *p*-GaSe/*n*-$In_2Se_3$ junctions

Figure 1a shows a schematic of the *p*-GaSe/*n*-$In_2Se_3$ heterojunction with two graphene electrodes (left) and an optical image of a

[1]School of Physics and Astronomy, University of Nottingham, Nottingham NG7 2RD, UK. [2]State Key Laboratory of Superlattices and Microstructures, Institute of Semiconductors, Chinese Academy of Sciences, 100083 Beijing, China. [3]Frantsevich Institute for Problems of Materials Science, The National Academy of Sciences of Ukraine, Chernivtsi Branch, Chernivtsi 58001, Ukraine. ✉email: shihong.xie@nottingham.ac.uk; amalia.patane@nottingham.ac.uk

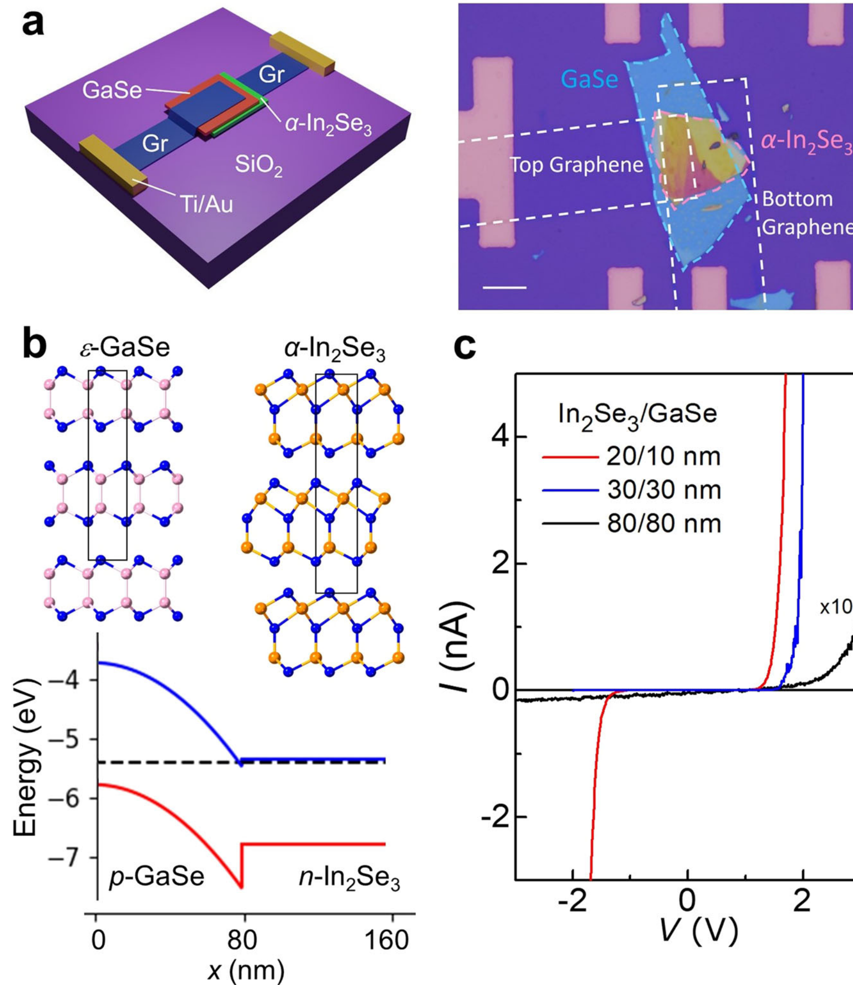


**Fig. 1 Graphene-contacted *p*-GaSe/*n*-$In_2Se_3$ heterojunctions.** **a** Left: Schematic of a graphene contacted *p*-GaSe/*n*-$In_2Se_3$ junction. Right: Optical image of a device with $\alpha$-$In_2Se_3$ and $\varepsilon$-GaSe flakes with thickness of 20 nm and 10 nm, respectively. Scale bar: 10 µm. **b** Top: Crystal structure and unit cell of $\varepsilon$-GaSe and $\alpha$-$In_2Se_3$. Bottom: Band alignment and Fermi level (dashed line) of a bulk GaSe/$In_2Se_3$ junction in equilibrium. **c** Current–voltage *I*–*V* curves in the dark ($T = 300$ K) for 3 junctions with different layer thickness of the $\alpha$-$In_2Se_3$ (20, 30, 80 nm) and $\varepsilon$-GaSe (10, 30, 80 nm) flakes. The optical images for the 30/30 nm and 80/80 nm junctions are in Supplementary Fig. 3a and main text Fig. 4a, respectively.

typical device (right). The heterostructure is assembled by exfoliation and mechanical stamping of nanometre-thick vdW layers of $\alpha$-$In_2Se_3$ and $\varepsilon$-GaSe. Details of the fabrication and characterization of the layers by X-ray diffraction, Raman and photoluminescence (PL) spectroscopy are in the 'Methods' section and Supplementary Fig. 1. The layers are prepared from bulk Bridgman-grown crystals of $\alpha$-$In_2Se_3$ and $\varepsilon$-GaSe polytypes that have a hexagonal (2H) crystal structure (Fig. 1b). The single $\alpha$-$In_2Se_3$ vdW layer consists of five atomic layers stacked in the sequence Se–In–Se–In–Se (1 quintuplet layer (QL)). For $\varepsilon$-GaSe, each vdW layer consists of four closely packed, covalently bonded, monoatomic sheets in the sequence Se-Ga-Ga-Se. Along the *c*-axis, the primitive unit cells of $\alpha$-$In_2Se_3$ and $\varepsilon$-GaSe have lattice parameters of $c_{In2Se3} = 19.210$ Å and $c_{GaSe} = 15.949$ Å, respectively. Within each *a*-*b* plane, atoms form hexagons with lattice parameters $a_{In2Se3} = 4.031$ Å and $a_{GaSe} = 3.755$ Å. Although the crystals are intentionally undoped, both layers contain residual dopants. For bulk $\alpha$-$In_2Se_3$, Hall effect measurements indicate an electron density $n = 4.9 \times 10^{17}$ cm$^{-3}$ at $T = 300$ K due to the existence of native donors[33]. The *p*-GaSe crystals contain instead native acceptors and a low concentration of holes $p \sim 10^{13}$ cm$^{-3}$ at $T = 300$ K[34].

Figure 1b shows the type-II band alignment and built-in potential $eV_{bi} = 1.7$ eV of a *p*-GaSe/*n*-$In_2Se_3$ junction at equilibrium at $T = 300$ K, as derived by solving Poisson's equation and taking into account the band alignment and doping of the bulk layers. Here, we have used the electron affinities from the literature ($\chi_{GaSe} = 3.7$ eV[35], $\chi_{In2Se3} = 3.6$ eV[36]) and the measured band gap energy of the bulk crystals ($E_{GaSe} = 2.0$ eV, $E_{In2Se3} = 1.4$ eV, Supplementary Fig. 1). The depletion region of the junction extends primarily in the *p*-GaSe layer and is negligibly small in *n*-$In_2Se_3$ due to the much larger carrier concentration and dielectric constant of $In_2Se_3$ ($\varepsilon_{In2Se3} \sim 17$ and $\varepsilon_{GaSe} \sim 6$)[37,38]. As shown in Fig. 1c, the room temperature ($T = 300$ K) current–voltage (*I*–*V*) characteristics are asymmetric with respect to the polarity of the applied voltage with a rectification ratio of up to 1000 at $V = \pm 2$ V (Fig. 1c, blue curve). The current density remains small in both forward and reverse bias. Although the *I*-*V* curves of the junctions appear qualitatively similar to those of a traditional *pn*-junction, important differences emerge when we examine devices with thin layers (Fig. 1c). As shown in Fig. 1c, with decreasing layer thickness the current in both forward and reverse bias tends to increase and the *I*-*V*s become more symmetric with respect to the polarity of the applied voltage. These differences can arise from a qualitative change in the transport mechanisms. In a bulk-like junction,

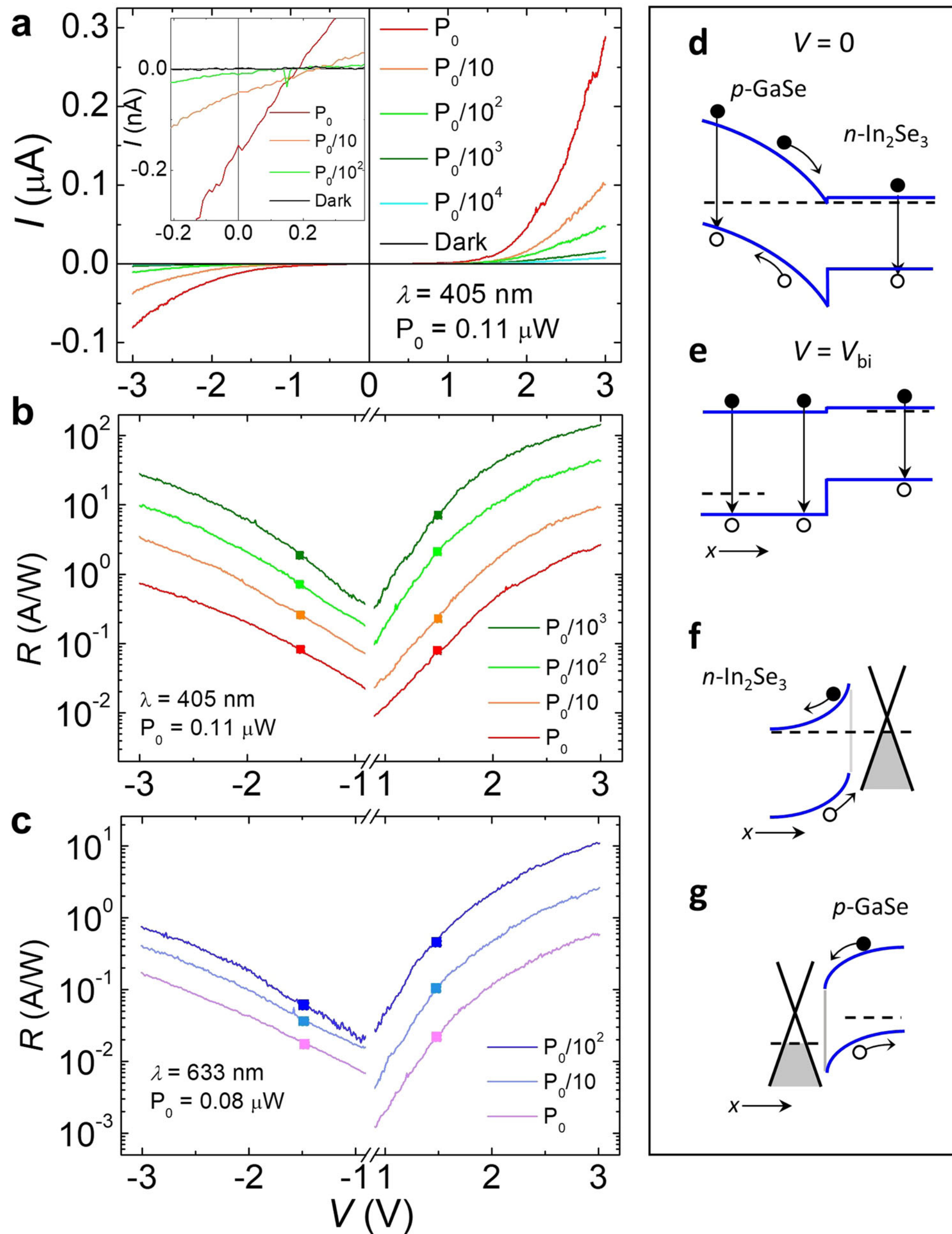


**Fig. 2 Heterojunctions under light illumination.** **a** Current–voltage $I$–$V$ characteristics of a graphene/$p$-GaSe/$n$-$In_2Se_3$/graphene junction in the dark and under illumination with $\lambda = 405$ nm and different powers ($T = 300$ K, $P_0 = 0.11$ μW). Inset: $I$–$V$ curves near zero bias. **b**, **c** Photoresponsivity ($R$) versus $V$ at different powers for **b** $\lambda = 405$ nm ($P_0 = 0.11$ μW) and **c** $\lambda = 633$ nm ($P_0 = 0.08$ μW) at $T = 300$ K. Square dots illustrate that the value of $R$ in forward bias is larger than that in reverse bias. **d**–**g** Band alignment at the **d**, **e** GaSe/$In_2Se_3$, **f** $In_2Se_3$/graphene, and **g** graphene/GaSe interfaces. For the GaSe/$In_2Se_3$ interface, the alignment is shown at **d** equilibrium and **e** $V = V_{bi}$, where $eV_{bi}$ is the built-in potential at the GaSe/$In_2Se_3$ junction.

regions depleted of free carriers form on either side of the junction, thus generating built-in potentials. Carrier transport across the junction occurs by diffusion. However, for junctions composed of thin $p$- and $n$-type semiconductors, tunnelling-assisted interlayer recombination of majority carriers can increase the current in forward bias[32]; also, charge transport via tunnelling across a thin barrier between the two graphene electrodes and/or leakage via defects in the junction can dominate the current in both forward and reverse bias. Further differences emerge when we consider the photoresponse (Figs. 2–5), as discussed below.

Figure 2a shows the $I$–$V$ characteristics of a junction under illumination with unfocused laser light of energy $h\nu = 3.06$ eV ($\lambda = 405$ nm). In both forward and reverse bias, the current increases with increasing incident power $P_i$. A photovoltaic response is also observed with a short-circuit current ($V = 0$) of up to 0.15 nA for $P_i = 0.11$ μW (inset of Fig. 2a). Figure 2b, c show the dependence of the photoresponsivity $R = \Delta I/P_i$, on $V$ and $P_i$ under unfocussed light illumination with $\lambda = 405$ nm and $\lambda = 633$ nm, respectively. Here, $\Delta I = I_{light} - I_{dark}$ is the photocurrent. A large value of $R$ of up to 145 A $W^{-1}$ is observed at $V = +3$ V at $\lambda = 405$ nm and $P_i = 0.11$ nW. The corresponding values of the external quantum efficiency (EQE = $Rh\nu/e$) and detectivity ($D^* = R(A/2eI_{dark})^{1/2}$) are EQE = $4.4 \times 10^2$ and $D^* = 1.0 \times 10^{13}$ Jones, where $A = 20$ $\mu m^2$ is the area of the device. Also, we estimate the noise equivalent power (NEP) as NEP $= \frac{I_{noise}}{R}$, where $I_{noise}$ is the noise current derived from the standard deviation in the temporal fluctuations of the dark current. For $R = 145$ A/W and $I_{noise} =$

$4.8\times10^{-12}$ A, NEP $= 3.3\times10^{-14}$ W. The corresponding signal-to-noise ratio is SNR $= \frac{I_{signal}}{I_{noise}} = 6.0\times10^4$. For all applied voltages, $R$ is approximately one order of magnitude larger at $\lambda = 405$ nm than at $\lambda = 633$ nm, reflecting an increased optical absorption of the layers at shorter wavelengths. Furthermore, the junction can be switched between on and off states in a reproducible manner with rise and decay times of $\tau \sim 100$ ms and without any photo-induced memory effects and/or hysteresis in the $I$–$V$s (Supplementary Fig. 2). The trapping/detrapping of charge carriers due to the disordered potential of the heterostructure and/or crystal defects tend to slow down the photoresponse. We estimate the bandwidth from the photocurrent rise time/decay time, e.g. $f_{3dB} = 0.35/\tau = 4.5$ Hz and $\Delta f = f_{3dB}/0.886 = 5.1$ Hz. Here, $f_{3dB}$ is the 3-dB bandwidth of the detector. This is defined as the frequency at which the photocurrent decreases by 3 dB of its maximum value[39]. Using these parameters to estimate the detectivity, we find $D^* = \frac{\sqrt{A\Delta f}}{NEP} \sim 3\times10^{10}$ Jones. This is smaller than the value of $D^* \sim 10^{13}$ Jones, as derived from $D^* = R(A/2eI_{dark})^{1/2}$, which assumes that the total noise is dominated by the shot noise from the dark current.

We have investigated junctions with different thickness of the layers (Supplementary Figs. 3–5) and all revealed a similar behaviour with a photoresponse that extends from the NIR (near-infrared) to the VIS (visible) and the UV range even without any applied voltage. Figure 3 shows the dependence of the responsivity on the photon wavelength at $V = 0$ for a junction based on a relatively thin (~60 nm) $p$-GaSe/$n$-$In_2Se_3$ junction. It can be seen that the photoresponse increases with decreasing photon wavelength, with a stronger increase observed at energies larger than the band gap energy of GaSe. Although the responsivity remains high in all devices, the detectivity and photovoltaic response tend to become weaker in the shorter junctions due to larger dark currents and shorter depletion regions.

The responsivity of all devices is comparable or higher than the values for photodetectors based on individual flakes of GaSe[21,24,28] or $In_2Se_3$[25,26,40–42]. Also, $pn$-heterojunctions based on GaSe from this work and the literature (Supplementary Table 1) tend to have a photoresponsivity that is higher under forward bias conditions. This behaviour differs from that of a traditional diode. In the latter, the photocurrent is larger in reverse bias as the spatial extent of the space charge region and the magnitude of the electric field increase with increasing reverse bias, thus facilitating the separation of photocreated electrons and holes and their collection at the electrodes. However, for our junctions, as the forward voltage increases above $V \sim +1.5$ V (Fig. 2a–c), the photocurrent and photoresponse can become larger than that in

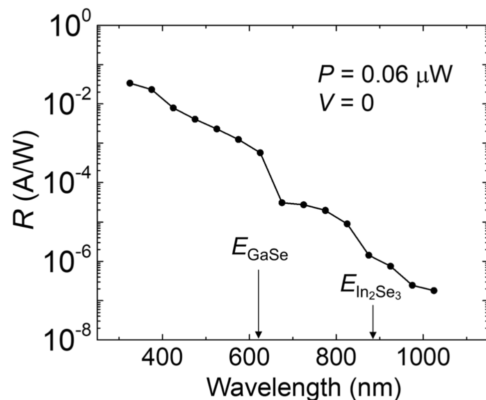


**Fig. 3 Wavelength-dependent photoresponsivity.** Dependence of the photoresponsivity ($R$) on the photon wavelength for a graphene contacted $p$-GaSe/$n$-$In_2Se_3$ junction (GaSe/$In_2Se_3$ thickness ~30/30 nm) at $V = 0$ and power $P = 0.06$ μW. The arrows indicate the band gap energies of GaSe and $In_2Se_3$, respectively.

reverse bias. This behaviour is observed for different powers and laser wavelengths. Thus, the photoresponse cannot arise just from the photon-current conversion at the $In_2Se_3$/GaSe interface (Fig. 2d, e) and additional mechanisms should be considered at large positive $V$. To examine these mechanisms, we calculate the energy band alignment for a graphene/$p$-GaSe/$n$-$In_2Se_3$/graphene junction at $V = 0$ and under forward bias (see Supplementary Note 1 and Supplementary Fig. 6). We assume that the layers are depleted and that the $pn$-junction and Schottky junctions can be treated in isolation. From the electron affinity of the layers ($\chi_{GaSe} = 3.7$ eV[35], $\chi_{In2Se3} = 3.6$ eV[36] and $\chi_{Graphene} = 4.5$ eV[43]) and their doping, we estimate a Schottky barrier height of $\Phi_{In2Se3} = 1.06$ eV and $\Phi_{GaSe} = 1.04$ eV at the $In_2Se_3$/graphene and GaSe/graphene interfaces, respectively (Supplementary Table 2). The depletion regions of the junction extend primarily in the $p$-GaSe layer and are much smaller in $n$-$In_2Se_3$ due to the larger carrier concentration of $In_2Se_3$. When the junction is forward biased, the photocurrent can increase due to an enhanced contribution to the photoresponse from the separation of electron-hole pairs at the $In_2Se_3$/graphene (Fig. 2f) and GaSe/graphene (Fig. 2g) interfaces. Thus, in forward bias, both interfaces behave as reverse-biased Schottky contacts and can contribute to the $I$–$V$ with a photocurrent that has the same polarity as the dark current. Since the $In_2Se_3$ layer has a band gap energy $E_{In2Se3} \approx 1.4$ eV, significantly smaller than that of GaSe (Supplementary Fig. 1), the contribution from the $In_2Se_3$/graphene interface becomes dominant for photon energies below the band gap of GaSe ($E_{GaSe} = 2.0$ eV). In summary, the three interfaces of the graphene/$p$-GaSe/$n$-$In_2Se_3$/graphene heterostructure contribute to the photodetection. Although our model does not capture the evolution of the multi-layer structure as the layer thickness decreases down to a few nanometres, it illustrates that the built-in potential at the three interfaces plays a critical role in the photoresponsivity. This is further examined by spatial mapping of the photoresponse of junctions with different thickness.

## Scanning photocurrent microscopy

We used a confocal optical microscope to obtain a photocurrent map of the junctions by focusing and scanning a laser beam onto the layer plane of the samples. Figure 4a shows the bias-dependence of the photocurrent under focused laser excitation of a junction (inset of Fig. 4a). The corresponding $I$–$V$ curves under unfocused laser excitation are shown in Fig. 2a. Figure 4b–f show the corresponding photocurrent maps of the device acquired under a range of bias voltages. To distinguish the different areas of the heterojunction, in each map, the GaSe, $In_2Se_3$ and graphene layers are marked by dashed lines. At zero bias (Fig. 4b), the photocurrent signal arises from the area where the four layers (top and bottom graphene, GaSe and $In_2Se_3$) of the heterostructure overlap, indicating a built-in potential at the $pn$-junction and efficient extraction of photo-created carriers at the two graphene electrodes.

Some general considerations can be drawn from the inspection of the photocurrent maps of several junctions. For example, by comparing the photocurrent maps of Fig. 4, it can be seen that at $V = \pm1$ V (Fig. 4c, e) the amplitude of the photocurrent signal in forward bias is smaller than that in reverse bias; in contrast, at $V = \pm2$ V (Fig. 4d, f), the photocurrent in forward bias is larger than in reverse bias. This behaviour is illustrated by the bias dependence of the photocurrent in Fig. 4a and is consistent with the $I$–$V$ characteristics acquired under unfocused laser light in Fig. 2. The responsivity values in the focused and unfocused mode versus the laser power density are plotted in Supplementary Fig. 7. The data show that the responsivity in the focused laser mode is in line with data for the unfocused mode. In particular, the value of $R$ tends to decrease with increasing laser power due to the increase in carrier recombination rate for increasing densities of

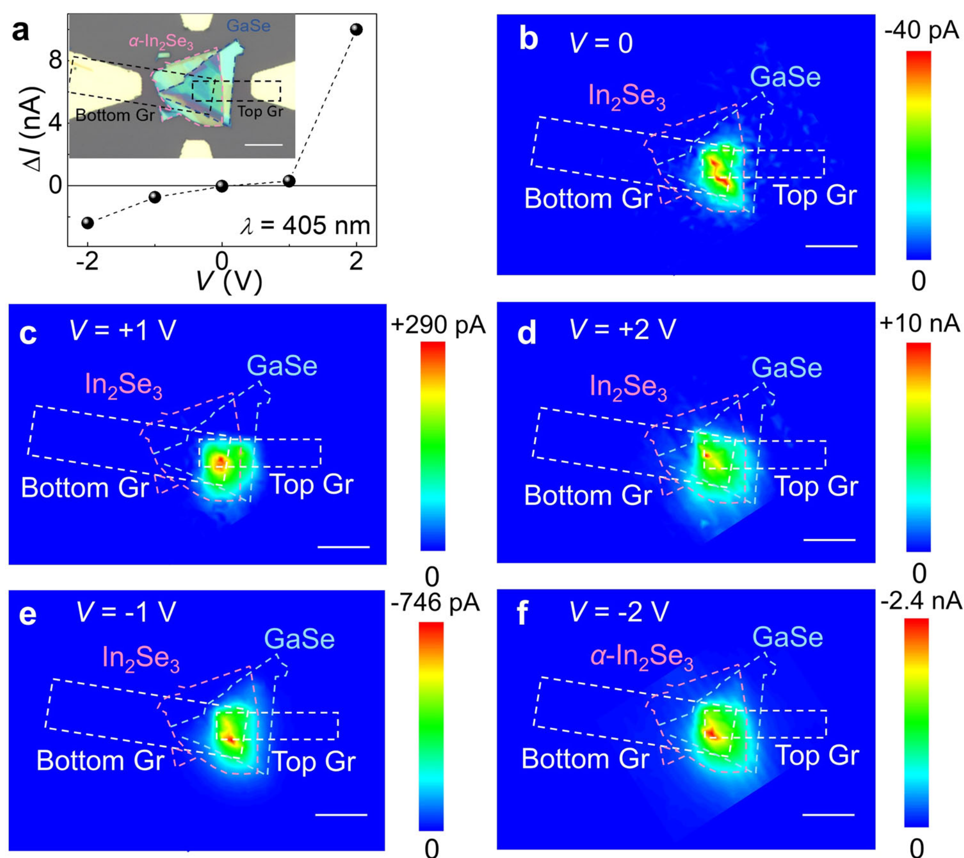


**Fig. 4 Photocurrent maps. a** Room temperature ($T = 300$ K) photocurrent ($\Delta I$) versus $V$ under a focused laser beam ($\lambda = 405$ nm and $P = 0.75$ μW) for a bulk (thickness of $In_2Se_3$/GaSe ~80/80 nm) junction. The corresponding $I$–$V$ curves under unfocused laser light are in Fig. 2. The data correspond to the largest value of $\Delta I$ at each $V$. Inset: optical image of the device. Scale bar: 10 μm. **b**–**f** Photocurrent maps under bias $V = 0, +1, +2, -1, -2$ V. The laser beam ($\lambda = 405$ nm and $P = 0.75$ μW) is focussed by the microscope objective to a spot size of around 1 μm. Scale bar: 10 μm.

photogenerated carriers[25–28]. Although the behaviour of junctions with different layer thickness is qualitatively similar, in the thinner junctions the photoresponsivity becomes more symmetric with respect to a reversal of bias polarity (Supplementary Fig. 4).

In general, the photocurrent can be non-uniform in the plane of the junction, revealing hot spots of photoresponse. These can arise not only from the non-uniformity of the individual layers, but also from their interlayer coupling, which can vary in the layer plane due to defects and/or surface roughness, and a non-uniform spatial distribution of dopants at each interface. Thus, the relative contribution of the three vdW interfaces (e.g. GaSe/$In_2Se_3$, GaSe/graphene and $In_2Se_3$/graphene) to a photocurrent map can vary from device to device (Supplementary Figs. 3–5). Figure 5 illustrates a junction in which the dominant contribution to the photocurrent arises from a large overlapping area between GaSe and graphene. Figure 5a shows the bias-dependence of the photocurrent under focused laser excitation of the junction (inset of Fig. 5a). As the carrier density of $In_2Se_3$ is much larger than GaSe, the depletion region extends primarily in the $p$-GaSe layer and is negligibly small in $n$-$In_2Se_3$. Similarly, we expect a charge redistribution at the GaSe/graphene interface, leading to the formation of a GaSe/graphene Schottky contact. The separation of photocreated carriers at the GaSe/graphene interface generates a photocurrent with opposite sign to that of the $pn$-junction at $V = 0$ (Fig. 5b) and same sign in forward and reverse bias (Fig. 5c, d). For this junction, it can be seen that the photocurrent signal is observed outside the region of overlap between the two graphene layers, where the electric field should be effectively zero. This current can arise from a non-uniform electric field potential in the layer plane and a temperature gradient induced by non-uniform heating under the focused laser beam through the photo-thermoelectric effect[44,45].

In summary, these photodetectors enable an efficient collection of photo-generated carriers resulting into a high photoresponsivity. Bulk junctions are more preferable for photodetection as the dark current is lower in both forward and reverse bias, leading to a large detectivity. In reverse bias, the low dark current indicates a small leakage current due to negligible thermal excitation of carriers across the band gaps of GaSe and $In_2Se_3$; in forward bias, the low dark current suggests instead a small recombination current. The mechanisms for photodetection in forward bias and the recombination of carriers are further examined in the following section.

## Carrier recombination and its bias dependence

We investigated the recombination of carriers by conducting electroluminescence (EL) and PL experiments under an applied voltage. No EL signal was detected in these junctions. However, a PL signal from both GaSe and $In_2Se_3$ was measured and found to be sensitive to the applied bias. Figure 6a shows the RT PL spectra at $V = 0$ for the junction of Figs. 2 and 4. The PL spectrum comprises a weak band edge emission from the $In_2Se_3$ (band I) and GaSe (band III) layers, and a broad, structured emission (band II) centred at around 1.8 eV, at energies between band I and III, with amplitude that tends to saturate with increasing laser power. This emission is spatially localized (see micro-PL imaging in Fig. 6b), indicative of an extrinsic carrier recombination in GaSe.

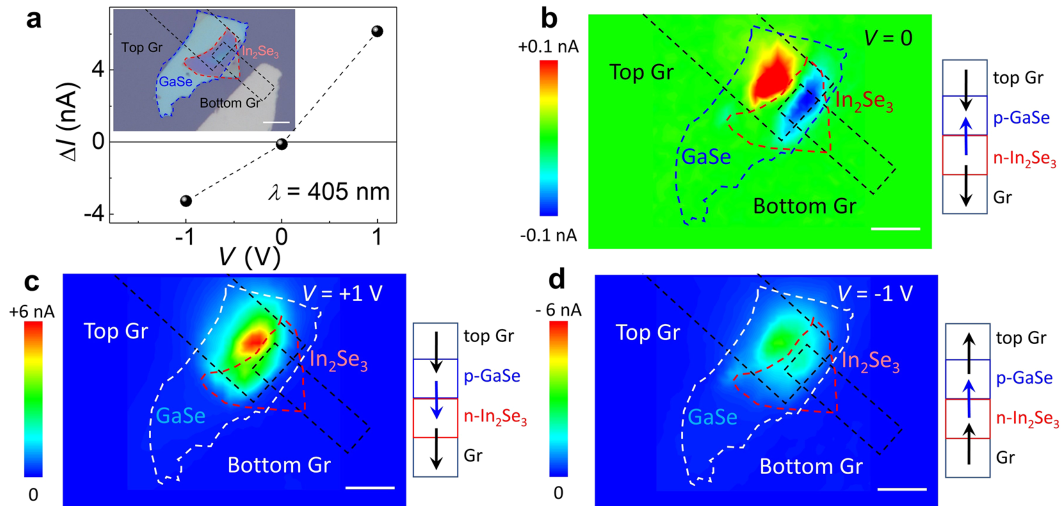


**Fig. 5 Schottky contacts in graphene-contacted *p*-GaSe/*n*-$In_2Se_3$ heterojunctions. a** Room temperature ($T = 300$ K) photocurrent ($\Delta I$) versus $V$ under a focused laser beam ($\lambda = 405$ nm and $P = 5$ μW) for a junction (thickness of $In_2Se_3$/GaSe ~60/40 nm). The data correspond to the largest value of $\Delta I$ at each $V$. Inset: optical image of the device. Scale bar: 10 μm. **b**–**d** Room temperature ($T = 300$ K) photocurrent ($\Delta I$) maps at **b** $V = 0$, **c** $+1$ V and **d** $-1$ V. The laser beam ($\lambda = 405$ nm and $P = 5$ μW) has a spot size of about 1 μm. Scale bar: 10 μm. The right insets in **b**–**d** illustrate the direction of the current across the three interfaces of the heterostructure.

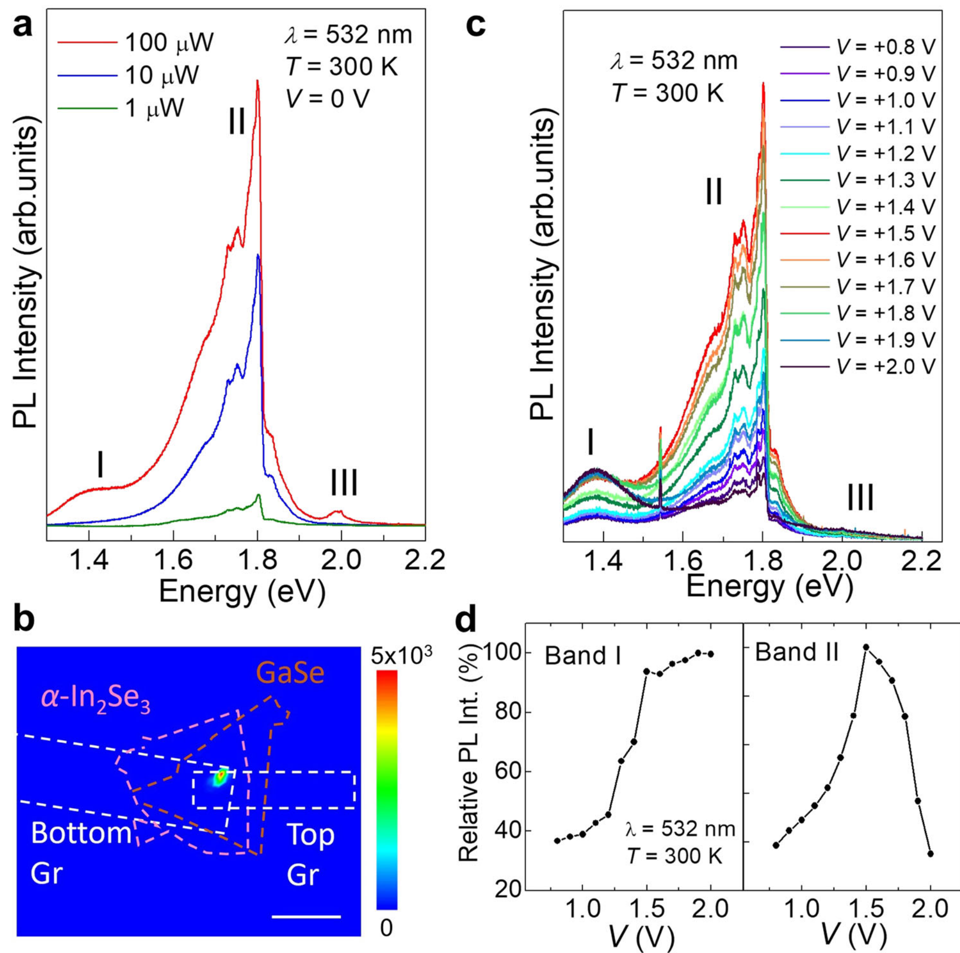


**Fig. 6 Bias-dependent photoluminescence. a** Photoluminescence (PL) spectra of the *p*-GaSe/*n*-$In_2Se_3$ photodetector shown in Figs. 2 and 4 for different excitation powers, showing three main bands: band I, II, and III. The PL emission arises from a localized region of the junction, as probed by the PL intensity map in **b**. Scale bar: 10 μm. **c** PL spectra of the photodetector for different voltages $V$. **d** $V$-dependence of the PL intensity of bands I and II ($T = 300$ K, $\lambda = 532$ nm).

The energy peak position of band II does not reveal any significant shift with the applied bias. However, the intensity of this band is modulated by the applied voltage, reaching a maximum at $V \sim 1.5$ V (Fig. 6c, d). As $V$ increases, the built-in electric field at the $In_2Se_3$/GaSe interface decreases and electron–hole recombination becomes more favourable. On the other hand, as $V$ increases, the electric field at the graphene/GaSe interface also increases, thus causing a bias-induced quenching of the PL emission at large $V$. The quenching of the PL emission over a wide range of biases is pronounced (~100%), supporting an effective charge separation and light-current conversion at the $In_2Se_3$/GaSe and GaSe/graphene interfaces. We note that the bias-dependence of the PL emission due to $In_2Se_3$ (band I, Fig. 6d) is slightly different. Although the initial increase of PL intensity with increasing $V$ is observed also in this case, this is then followed by a saturation of the PL signal at large $V$. We assign this different behaviour to the larger carrier concentration in $In_2Se_3$ ($n \sim 10^{17}$ cm$^{-3}$) compared to that in GaSe ($p \sim 10^{13}$ cm$^{-3}$). Combined with a large dielectric contrast of $In_2Se_3$ ($\varepsilon_{In2Se3} \sim 17$[37,38]), this leads to more effective screening of the electric field in $In_2Se_3$.

While the separation of charges at three interfaces can explain both the photoresponse and carrier recombination, the origin of band II remains unclear. In particular, the observation of this band is suggestive of a recombination channel that is not beneficial for photodetection. Theoretical studies of the energetics of crystal defects in GaSe have shown that acceptor levels due to Ga vacancies ($V_{Ga}$) have energies at approximately 0.2 eV above the valence band (VB) edge, while interstitial Ga ($Ga_i$) create donor levels at 0.2 eV below the conduction band (CB) edge[46]. Large scale defects, including clusters of point defects and cracks/local stacking faults, can also form as the result of mechanical stress applied to a crystal during fabrication[47]. These can induce localized regions with enhanced PL emission in the range 1.7–2.0 eV[48], as observed in our micro-PL imaging studies (Fig. 6b). Similar, but broader extrinsic PL emissions can be generated via controlled thermal annealing of individual flakes of GaSe (see thermal annealing studies in Supplementary Fig. 8). The sensitivity of these junctions to charges trapped by defects of GaSe indicates that efficient optoelectronic devices based on this material require an optimization of the fabrication process. A crucial requirement is the in-plane spatial homogeneity of the layers, which can affect interlayer coupling and band alignments. Furthermore, GaSe can oxidize in air leading to morphological and chemical changes of its surface. Thus, an effective passivation strategy should also be adopted to mitigate these effects. To avoid the oxidation of GaSe during our device studies, all electrical studies were conducted in vacuum and at laser powers that avoid light-induced changes of GaSe. The stability tests of our devices under these conditions are shown in Supplementary Fig. 9. The measured current remains stable over time, switching between high to low (dark current) values in response to the impinging laser power.

In conclusion, we have exploited the vdW interfaces of the graphene/$p$-GaSe/$n$-$In_2Se_3$/graphene heterostructure to fabricate high-responsivity UV photodetectors. Their operation exploits the optical absorption of the metal chalcogenide layers and the built-in potential at the three vdW interfaces of the heterostructure. The junctions can have high photoresponsivity and low dark current in both forward and reverse biases, and without any externally applied bias. Thus, these multi-layer vdW heterostructures could play a crucial role in the development of high performance 2D semiconductor-based devices for a broad range of applications. Scanning photocurrent microscopy revealed that the contribution of the three interfaces to the overall responsivity can differ from device to device due to the non-uniformity of the layers and their coupling. For example, defects can act as recombination centres in GaSe leading to a photoluminescence emission that is modulated by the applied voltage. Thus, these devices could be improved by optimization of their fabrication to reduce the contribution of crystal defects and optimize interlayer coupling. Further optimization of the layer thickness and doping, and scalable growth of the layers could also lead to optimal designs for even larger responsivity and detectivity, offering an alternative to conventional UV detection technologies.

## METHODS

### Materials and device fabrication

We used Bridgman-grown $\alpha$-$In_2Se_3$ and $\varepsilon$-GaSe crystals. The crystal structures of the $\alpha$-$In_2Se_3$ and $\varepsilon$-GaSe bulk crystals were determined from X-ray diffraction studies on a DRON-3M diffractometer. The room temperature PL emission of bulk $\alpha$-$In_2Se_3$ and $\varepsilon$-GaSe are centred at about 1.4 eV and 2.0 eV respectively. Chemical Vapour Deposition (CVD) graphene, exfoliated $\alpha$-$In_2Se_3$ and exfoliated $\varepsilon$-GaSe flakes form the graphene/$In_2Se_3$/GaSe/graphene heterostructure. The thicknesses of the GaSe and $\alpha$-$In_2Se_3$ flakes were estimated from their colour profiles in the optical images. Each heterostructure was assembled onto a $SiO_2$/$p$-Si substrate ($SiO_2$ layer thickness of 300 nm). For the stamping of the top and bottom graphene layers, we used a needle-assisted transfer process of patterned graphene microsheets, as described in ref. [49]. The bottom graphene flakes were first deposited onto the $SiO_2$/$p$-Si substrate with pre-patterned metal contacts (Au/Ti ~ 100 nm/10 nm) using a dry transfer method under ambient conditions. Flakes of $In_2Se_3$ and GaSe were exfoliated onto polydimethylsiloxane (PDMS) from a low-tack, low-residue tape and identified using transmission and reflection mode optical microscopy. Then, using a micromanipulator stage, an exfoliated flake of $\alpha$-$In_2Se_3$ on PDMS was aligned to the pre-deposited bottom graphene flake and brought into contact. The PDMS was then slowly retracted in order to deposit $\alpha$-$In_2Se_3$. A GaSe flake was stamped on top of the $In_2Se_3$ flake by the PDMS-assisted method mentioned above. Finally, the top graphene contact was aligned to the $In_2Se_3$/GaSe heterostructure and Au/Ti metal contact.

### Electrical, optical and microscopy measurements

Electrical and opto-electrical measurements were acquired using a Keithley 2400 Sourcemeter, an Agilent Technology B1500A Semiconductor Analyser and a lock-in amplifier (SR830) with a light chopper. Unfocused laser beams of wavelength $\lambda = 405$ nm and 633 nm were used for the photocurrent measurements. The continuous spectrum from NIR to VIS and UV monochromatic illumination was provided by a Fianium WhiteLase Supercontinuum Laser Source and a Xe lamp, respectively. The output laser wavelength was tuned by an Omni-λ300 monochromator. For photocurrent mapping experiments, a focused laser beam ($\lambda = 405$ nm or 425 nm and spot diameter $d \approx 1$ μm) was used. All transport measurements were conducted in a vacuum environment (~$10^{-6}$ mbar). The experimental setup for the micro-Raman and micro-PL spectroscopy studies at room temperature comprised of a frequency doubled Nd:$YVO_4$ laser ($\lambda = 532$ nm and $d \approx 1$ μm), an $x$–$y$–$z$ motorized stage and an optical confocal microscope system equipped with a 0.5-m long monochromator with 1200 g/mm and 150 g/mm gratings. The signal was detected by a Si-charge-coupled device camera. The optical studies were performed at low excitation power to avoid excessive heating. The laser annealing studies were conducted using this set up and different laser powers.

## DATA AVAILABILITY

The data that support the findings of this study are available upon reasonable request from the authors.

## CODE AVAILABILITY

The codes that support the findings of this study are available from the corresponding author upon reasonable request.

Received: 7 March 2022; Accepted: 24 August 2022;
Published online: 08 September 2022

## REFERENCES

1. Monroy, E., Omnès, F. & Calle, F. Wide-bandgap semiconductor ultraviolet photodetectors. *Semicond. Sci. Technol.* **18**, R33–R51 (2003).
2. Wan, X. et al. A self-powered high-performance graphene/silicon ultraviolet photodetector with ultra-shallow junction: breaking the limit of silicon? *npj 2D Mater. Appl* **1**, 4 (2017).
3. Salvato, M. et al. Time response in carbon nanotube/Si based photodetectors. *Sens. Actuator A Phys.* **292**, 71–76 (2019).
4. Tran, H. et al. Si-based GeSn photodetectors toward mid-infrared imaging applications. *ACS Photonics* **6**, 2807–2815 (2019).
5. Razeghi, M. Short-wavelength solar-blind detectors-status, prospects, and markets. *Proc. IEEE* **90**, 1006–1014 (2002).
6. Li, Q. et al. Gas-mediated liquid metal printing toward large-scale 2D semiconductors and ultraviolet photodetector. *npj 2D Mater. Appl* **5**, 36 (2021).
7. Lin, C.-H. et al. A flexible solar-blind 2D boron nitride nanopaper-based photodetector with high thermal resistance. *npj 2D Mater. Appl* **2**, 23 (2018).
8. Xie, C. et al. Recent progress in solar-blind deep-ultraviolet photodetectors based on inorganic ultrawide bandgap semiconductors. *Adv. Funct. Mater.* **29**, 1806006 (2019).
9. Lv, Q., Yan, F., Wei, X. & Wang, K. High-performance, self-driven photodetector based on graphene sandwiched GaSe/$WS_2$ heterojunction. *Adv. Opt. Mater.* **6**, 1700490 (2018).
10. Long, M., Wang, P., Fang, H. & Hu, W. Progress, challenges, and opportunities for 2D material based photodetectors. *Adv. Funct. Mater.* **29**, 1803807 (2019).
11. George, A. et al. Giant persistent photoconductivity in monolayer $MoS_2$ field-effect transistors. *npj 2D Mater. Appl* **5**, 15 (2021).
12. Wang, X., Cheng, Z., Xu, K., Tsang, H. K. & Xu, J.-B. High-responsivity graphene/silicon-heterostructure waveguide photodetectors. *Nat. Photonics* **7**, 888–891 (2013).
13. Jariwala, D. et al. Near-unity absorption in van der waals semiconductors for ultrathin optoelectronics. *Nano Lett.* **16**, 5482–5487 (2016).
14. Wong, J. et al. High photovoltaic quantum efficiency in ultrathin van der Waals heterostructures. *ACS Nano* **11**, 7230–7240 (2017).
15. Wu, F. et al. High efficiency and fast van der Waals hetero-photodiodes with a unilateral depletion region. *Nat. Commun.* **10**, 4663 (2019).
16. Novoselov, K. S., Mishchenko, A., Carvalho, A. & Castro Neto, A. H. 2D materials and van der Waals heterostructures. *Science* **353**, aac9439 (2016).
17. Fang, H. & Hu, W. Photogating in low dimensional photodetectors. *Adv. Sci.* **4**, 1700323 (2017).
18. Yan, F., Hu, C., Wang, Z., Lin, H. & Wang, K. Perspectives on photodetectors based on selenides and their van der Waals heterojunctions. *Appl. Phys. Lett.* **118**, 190501 (2021).
19. Chen, Y. et al. Unipolar barrier photodetectors based on van der Waals heterostructures. *Nat. Electron.* **4**, 357–363 (2021).
20. Song, Q. et al. Moiré perovskite photodetector toward high-sensitive digital polarization imaging. *Adv. Energy Mater.* **11**, 2100742 (2021).
21. Hu, P., Wen, Z., Wang, L., Tan, P. & Xiao, K. Synthesis of few-layer GaSe nanosheets for high performance photodetectors. *ACS Nano* **6**, 5988–5994 (2012).
22. Chu, J. et al. High-performance ultraviolet photodetector based on a few-layered 2D $NiPS_3$ nanosheet. *Adv. Funct. Mater.* **27**, 1701342 (2017).
23. Wang, F. et al. 2D library beyond graphene and transition metal dichalcogenides: a focus on photodetection. *Chem. Soc. Rev.* **47**, 6296–6341 (2018).
24. Kim, W. et al. Photoresponse of graphene-gated graphene-GaSe heterojunction devices. *ACS Appl. Nano Mater.* **1**, 3895–3902 (2018).
25. Xie, S. et al. Ferroelectric semiconductor junctions based on graphene/$In_2Se_3$/graphene van der Waals heterostructures. *2D Mater.* **8**, 045020 (2021).
26. Island, J. O., Blanter, S. I., Buscema, M., van der Zant, H. S. & Castellanos-Gomez, A. Gate controlled photocurrent generation mechanisms in high-gain $In_2Se_3$ phototransistors. *Nano Lett.* **15**, 7853–7858 (2015).
27. Cao, Y. et al. Strong enhancement of photoresponsivity with shrinking the electrodes spacing in few layer GaSe photodetectors. *Sci. Rep.* **5**, 8130 (2015).
28. Sorifi, S., Moun, M., Kaushik, S. & Singh, R. High-temperature performance of a GaSe nanosheet-based broadband photodetector. *ACS Appl. Electron. Mater.* **2**, 670–676 (2020).
29. Ning, J. et al. Self-driven photodetector based on a GaSe/$MoSe_2$ selenide van der Waals heterojunction with the hybrid contact. *Appl. Phys. Lett.* **117**, 163104 (2020).
30. Jariwala, D. et al. Gate-tunable carbon nanotube-$MoS_2$ heterojunction p-n diode. *Proc. Natl. Acad. Sci. USA* **110**, 18076–18080 (2013).
31. Jariwala, D. et al. Hybrid, gate-tunable, van der Waals p-n heterojunctions from pentacene and $MoS_2$. *Nano Lett.* **16**, 497–503 (2016).
32. Lee, C. H. et al. Atomically thin p-n junctions with van der Waals heterointerfaces. *Nat. Nanotechnol.* **9**, 676–681 (2014).
33. Zaslonkin, A., Kovalyuk, Z. & Mintyanskii, I. Electrical properties of $In_2Se_3$ layered crystals doped with cadmium, iodine, or copper. *Inorg. Mater.* **43**, 1271–1274 (2007).
34. Katerinchuk, V. N., Kovalyuk, Z. D., Netyaga, V. V. & Betsa, T. V. Heterojunctions produced from the layered semiconductors $SnS_{1.9}Se_{0.1}$ and GaSe<Cd>. *Inorg. Mater.* **37**, 336–338 (2001).
35. Jaegermann, W., Klein, A. & Pettenkofer, C. in *Electron Spectroscopies Applied to Low-Dimensional Materials* 317–402 (Springer, 2002).
36. Drapak, S., Kovalyuk, Z., Netyaga, V. & Orletskii, V. On the mechanisms of current transfer in n-$In_2Se_3$-p-GaSe heterostructures. *Tech. Phys. Lett.* **28**, 707–710 (2002).
37. Errandonea, D., Segura, A., Muñoz, V. & Chevy, A. Effects of pressure and temperature on the dielectric constant of GaS, GaSe, and InSe: Role of the electronic contribution. *Phys. Rev. B* **60**, 15866–15874 (1999).
38. Wu, D. et al. Thickness-dependent dielectric constant of few-layer $In_2Se_3$ nanoflakes. *Nano Lett.* **15**, 8136–8140 (2015).
39. Kaushik, S. & Singh, R. 2D layered materials for ultraviolet photodetection: a review. *Adv. Opt. Mater.* **9**, 2002214 (2021).
40. Jacobs-Gedrim, R. B. et al. Extraordinary photoresponse in two-dimensional $In_2Se_3$ nanosheets. *ACS Nano* **8**, 514–521 (2014).
41. Wu, G. et al. Visible to short wavelength infrared $In_2Se_3$-nanoflake photodetector gated by a ferroelectric polymer. *Nanotechnology* **27**, 364002 (2016).
42. Xu, K. et al. Optical control of ferroelectric switching and multifunctional devices based on van der Waals ferroelectric semiconductors. *Nanoscale* **12**, 23488–23496 (2020).
43. Mudd, G. W. et al. High broad-band photoresponsivity of mechanically formed InSe–graphene van der Waals heterostructures. *Adv. Mater.* **27**, 3760–3766 (2015).
44. Xu, X., Gabor, N. M., Alden, J. S., van der Zande, A. M. & McEuen, P. L. Photo-thermoelectric effect at a graphene interface junction. *Nano Lett.* **10**, 562–566 (2010).
45. Zhao, H. et al. Conjuncted photo-thermoelectric effect in ZnO-graphene nanocomposite foam for self-powered simultaneous temperature and light sensing. *Sci. Rep.* **10**, 11864 (2020).
46. Deak, P., Han, M., Lorke, M., Tabriz, M. F. & Frauenheim, T. Intrinsic defects of GaSe. *J. Phys. Condens. Matter* **32**, 285503 (2020).
47. Hopkinson, D. G. et al. Formation and healing of defects in atomically thin GaSe and InSe. *ACS Nano* **13**, 5112–5123 (2019).
48. Tonndorf, P. et al. Single-photon emitters in GaSe. *2D Mater.* **4**, 021010 (2017).
49. Bie, Y.-Q. et al. Site-specific transfer-printing of individual graphene microscale patterns to arbitrary surfaces. *Adv. Mater.* **23**, 3938–3943 (2011).

## ACKNOWLEDGEMENTS

This work was supported by the European Union's Horizon 2020 research and innovation programme Graphene Flagship Core 3, the Engineering and Physical Sciences Research Council (Grant No. EP/M012700/1), the Defence Science and Technology Laboratory (DSTL) and the University of Nottingham Propulsion Futures Beacon.

## AUTHOR CONTRIBUTIONS

A.P. and S.X. conceived the project and wrote the paper; S.X. fabricated the devices and performed the experiments, assisted by Mustaqeem Shiffa, Mujahid Shiffa, W.Z., and O.M.; Z.R.K and Z.D.K. grew and characterized the bulk GaSe and $In_2Se_3$ crystals; S.X. conducted the analysis of the data, assisted by Mustaqeem Shiffa, Mujahid Shiffa, A.P. and K.W.; all authors discussed the results.

## COMPETING INTERESTS

The authors declare no competing interests.

## ADDITIONAL INFORMATION

**Supplementary information** The online version contains supplementary material available at https://doi.org/10.1038/s41699-022-00338-0.

**Correspondence** and requests for materials should be addressed to Shihong Xie or Amalia Patanè.

**Reprints and permission information** is available at http://www.nature.com/reprints

**Publisher's note** Springer Nature remains neutral with regard to jurisdictional claims in published maps and institutional affiliations.

**Open Access** This article is licensed under a Creative Commons Attribution 4.0 International License, which permits use, sharing, adaptation, distribution and reproduction in any medium or format, as long as you give appropriate credit to the original author(s) and the source, provide a link to the Creative Commons license, and indicate if changes were made. The images or other third party material in this article are included in the article's Creative Commons license, unless indicated otherwise in a credit line to the material. If material is not included in the article's Creative Commons license and your intended use is not permitted by statutory regulation or exceeds the permitted use, you will need to obtain permission directly from the copyright holder. To view a copy of this license, visit http://creativecommons.org/licenses/by/4.0/.

© The Author(s) 2022